ADP-07-20/T660
HU-EP-07/62
LMU-ASC 73/07
DESY 07-219

arXiv:0801.1725v1 [hep-lat] 11 Jan 2008

ADP-07-20/T660, HU-EP-07/62, LMU-ASC 73/07, DESY 07-219

Vacuum structure revealed by over-improved stout-link smearing compared with the overlap analysis for quenched QCD

E.-M. Ilgenfritz*, D. Leinweber, and P. Moran
Special Research Centre for the Subatomic Structure of Matter (CSSM), Department of Physics, University of Adelaide, Adelaide SA 5005, Australia

K. Koller
Sektion Physik, Universität München, 80333 München, Germany

G. Schierholz
John von Neumann-Institut für Computing NIC, 15738 Zeuthen, Germany and Deutsches Elektronen-Synchrotron DESY, 22603 Hamburg, Germany

V. Weinberg
John von Neumann-Institut für Computing NIC, 15738 Zeuthen, Germany and Institut für theoretische Physik, Freie Universität Berlin, 14196 Berlin, Germany

(Dated: January 11, 2008)

A detailed comparison is made between the topological structure of quenched QCD as revealed by the recently proposed over-improved stout-link smearing in conjunction with an improved gluonic definition of the topological density on one hand and a similar analysis made possible by the overlap-fermionic topological charge density both with and without variable ultraviolet cutoff λ_{cut}. The matching is twofold, provided by fitting the density-density two-point functions on one hand and by a point-by-point fitting of the topological densities according to the two methods. We point out the similar cluster structure of the topological density for moderate smearing and 200 MeV $< \lambda_{cut} <$ 600 MeV, respectively. We demonstrate the relation of the gluonic topological density for extensive smearing to the location of the overlap zero modes and the lowest overlap non-zero mode as found for the unsmeared configurations.

PACS numbers: 11.15.Ha, 12.38.Gc, 12.38.Aw

I. INTRODUCTION

Massless overlap fermions [1, 2] have provided us with a fermionic definition of topological charge [3, 4]. This offers the advantage that, by truncating to the overlap modes with $|\lambda| < \lambda_{cut}$, the effect of ultraviolet filtering can be studied [5] without changing the gauge field itself. A broad study of different aspects of vacuum structure, so far for quenched QCD, has been published recently [6]. On the other hand, during the 80's procedures of cooling or smearing of gauge fields were proposed to exhibit the infrared structure of gauge fields [7, 8]. This has been considered with reservations because it is difficult to assess in which aspect the gauge field configuration could have changed under this procedure. The practitioners of cooling/smearing, in particular those who were focussing on vacuum structure in the form of extended, smooth (semiclassical) structures, have continued to improve their techniques: cooling with improved actions [9], restricted improved cooling [10] etc). Over-improved cooling [11, 12] has been applied in order to prevent instantons or other topological excitations from collapsing.

More recently, the concept of cooling/smearing has been modified in another direction, to make it differentiable with respect to the unsmeared field. The so-called stout-link smearing [13] makes it possible to evaluate the "force" for the molecular dynamics in non-quenched update algorithms with a fermionic action involving some form of "fat" (smeared) links substituting the original gauge links. The concept of over-improvement has also recently been applied to stout-link smearing [14].

* leave of absence from Humboldt-Universität zu Berlin, Institut für Physik, 12489 Berlin, Germany

In this paper, following Ref. [15] we want to characterize the subsequent mapping "link → stout link" as a particular relaxation scheme, eventually leading to a finally classical configuration. One obvious way to discuss this process is to record the local distribution of topological charge density expressed by an improved [16] gluonic definition of field strength and topological density. In this paper we shall compare the emergent structures with the topological density provided by the overlap definition [6] with different levels of ultraviolet filtering. Surprisingly, the overlap topological charge density without filtering, that recently has been found to form lower-dimensional structures [6, 17, 18], corresponds to few steps of smearing. This comparison will lead us to a one-to-one mapping of the ultraviolet cutoff λ_{cut} (mode truncation in the overlap picture) to the number of stout-link smearing iterations over a wide range of smearing iterations. In a similar spirit, the correspondence of APE smearing [19], Laplacian filtering [20] and the topological density filtered according to another Ginsparg-Wilson Dirac operator [21, 22] has been studied recently [23, 24].

Only a few iterations of stout-link smearing are necessary before structures become recognizable with the gluonic definition of the topological density, and these structures are surprisingly far from 4D extended, sign-coherent lumps, such that the topological density compares well with the unfiltered overlap definition. We have two criteria to establish this relation between smearing and filtering. First, it is the behavior of the two-point correlation function of the topological density that emerges from the respective definition. The second is the actual site-by-site difference of the topological density profile over a set of lattice configurations. The quality of the latter coincidence is surprisingly good, which supports the reliability of both methods to explore the vacuum structure.

Finally, however, this relation becomes loose because stout-link smearing turns the configurations into piecewise classical fields which apparently resemble instantons and anti-instantons. Although the coherence among the lowest overlap modes guarantees a relatively simple picture of the fermionic topological density and the ultraviolet filtered gluonic field strength with low cutoff λ_{cut} [6], there is no argument as to why the overlap picture should be in correspondence to a (linkwise) classical lattice configuration.

It is intriguing to see that the instanton-like structure that is revealed in this late stage of smearing corresponds to the overlap zero mode(s) and the lowest pair(s) of overlap non-zeromodes obtained for the respective unsmeared (equilibrium) configuration. A similar observation has already been made by Negele *et al.* [25]. In Ref. [18] some of us have presented a cluster analysis of individual eigenmodes of the overlap Dirac operator. It turns out that the moderate number of clusters that the zero and first non-zero modes consist of (at a level of scalar density below the peak values) are pointing towards the positions where instantons and anti-instantons appear later.

Our paper is organized as follows: in Section II we explain briefly the overlap operator and the stout-link smearing procedure, in Section III we describe the matching between smearing and ultraviolet filtering, according to the two-point correlator and according to a global fitting of the profile of charge. In Section IV we try to relate the clusters that both definitions exhibit to each other. In the final stadium of smearing we shall confront the emergent semiclassical lumps with the lowest eigenmodes (zero mode and lowest non-zero mode) of the original configurations. In Section V we draw conclusions and give an outlook.

II. TECHNICAL DETAILS

A. Configurations and the overlap definition of topological density

The configurations underlying this comparison stem from an extended investigation published in Ref. [6]. The configurations are taken from an ensemble of $16^3 \times 32$ quenched lattices generated with the tadpole improved Lüscher-Weisz action at $\beta = 8.45$.

The (massless) overlap Dirac operator is constructed for the Wilson-Dirac input kernel $D_W = M - \rho/a$, M being the massless Wilson-Dirac operator with $r = 1$, and $\rho = 1.4$. The corresponding

solution of the Ginsparg-Wilson relation reads as follows

$$D(0) = \frac{\rho}{a}\left(1 + D_W/\sqrt{D_W^\dagger D_W}\right) = \frac{\rho}{a}\left(1 + \gamma_5 \mathrm{sgn}(H_W)\right) \ , \tag{1}$$

with $H_W = \gamma_5 D_W$. Circa 150 overlap eigenmodes have been obtained per configuration. They have been used to construct ultraviolet smeared topological densities according to a cut-off $\lambda_{cut} = 200$ MeV, 400 MeV and 635 MeV. For half of the subset of 10 configurations particularly considered in the present study we have also calculated for Refs. [6, 18] the overlap topological density without mode truncation, the "all-scale" topological density.

The spectrum eventually consists of some zero modes, in addition to pairs of non-zero modes of globally vanishing chirality. The topological density can be formally obtained from the trace of the overlap Dirac operator [4]

$$q(x) = -\mathrm{tr}\left[\gamma_5\left(1 - \frac{a}{2}D(0;x,x)\right)\right] \ . \tag{2}$$

Using the spectral representation of the overlap Dirac operator, a family of ultraviolet filtered topological charge densities labelled by $q_{\lambda_{cut}}(x)$ can be obtained [5, 26],

$$q_{\lambda_{cut}}(x) = -\sum_{|\lambda|<\lambda_{cut}}\left(1 - \frac{\lambda}{2}\right)\psi_\lambda^\dagger(x)\gamma_5\psi_\lambda(x) \ . \tag{3}$$

The topological charge of each configuration fulfills the Atiyah-Singer index theorem [3]

$$Q = n_- - n_+ \ . \tag{4}$$

Note that the zero modes of any given configuration carry the same chirality.

In this paper we shall point out that the above-mentioned family of densities is well represented by the gluonic topological density after an appropriate number of iterations of stout-link smearing.

B. Over-improved stout-link smearing

In Refs. [14, 15] two of us have motivated the stout-link smearing with respect to a specific over-improved action. The concept of over-improved action arose from the observation that the Wilson one-plaquette action does not guarantee the stability of instantons [27]. Even with the Symanzik improved action including 1×1 plaquettes and 1×2 rectangular loops, for a classical instanton solution of size ρ_{inst} placed on the lattice, the action is obtained as

$$S^{inst} = \frac{8\pi^2}{g^2}\left[1 - \frac{17}{210}\left(\frac{a}{\rho_{inst}}\right)^4\right] \ . \tag{5}$$

Following Garcia Perez *et al.* [11], Ref. [14] proposes to modify the relative contribution of plaquette and rectangular terms, parametrized by a parameter ϵ. For the Symanzik action this reads as follows

$$S(\epsilon) = \beta\sum_x\sum_{\mu<\nu}\left[\frac{5-2\epsilon}{3}\left(1 - P_{\mu\nu}(x)\right) - \frac{1-\epsilon}{12}\left(1 - R_{\mu\nu}(x) + 1 - R_{\nu\mu}(x)\right)\right] \ , \tag{6}$$

interpolating between Wilson ($\epsilon = 1$) and Symanzik action ($\epsilon = 0$). As usual, $\beta = 6/g^2$. The plaquettes are denoted as

$$P_{\mu\nu} = \frac{1}{3}\mathrm{Re\ Tr}\ \left(U_{x,\mu}U_{x+\hat{\mu},\nu}U_{x+\hat{\nu},\mu}^\dagger U_{x,\nu}^\dagger\right)$$

and the traces of the rectangular loops as

$$R_{\mu\nu} = \frac{1}{3}\mathrm{Re\ Tr}\ \left(U_{x,\mu}U_{x+\hat{\mu},\mu}U_{x+2\hat{\mu},\nu}U^{\dagger}_{x+\hat{\nu}+\hat{mu},\mu}U^{\dagger}_{x+\hat{\nu},\mu}U^{\dagger}_{x,\nu}\right)\ .$$

With this action the instanton action behaves as

$$S^{inst} = \frac{8\pi^2}{g^2}\left[1 - \frac{\epsilon}{5}\left(\frac{a}{\rho_{inst}}\right)^2 + \frac{14\epsilon - 17}{210}\left(\frac{a}{\rho_{inst}}\right)^4\right]\ . \tag{7}$$

In Ref. [15] a value $\epsilon = -0.25$ was found to provide an instanton action almost independent of the radius for $\rho_{inst} > 1.5a$.

The stout-link iteration solves the equation of motion (without momentum)

$$U^{old}_{x\mu} \to U^{new}_{x\mu} = \exp\left(-\rho_{sm}\ \frac{\delta S(\epsilon)}{\delta U_{x\mu}}\right)\ U^{old}_{x\mu} \tag{8}$$

in parallel, with a "time step" ρ_{sm}. No projection onto the group $SU(3)$ is required in distinction to APE smearing. The derivative is the traceless antihermitean part of a sum of untraced loops

$$\frac{\delta S(\epsilon)}{\delta U_{x\mu}} = \frac{5-2\epsilon}{3}\sum(\text{1x1 loops touching } U) + \frac{1-\epsilon}{12}\sum(\text{1x2 + 2x1 loops touching } U)_{|\text{antiherm traceless}}$$

with $U_{x\mu}$ in the leftmost position. This method has been discussed in Ref. [15] with respect to the two-point correlator of the topological density. The differences between quenched and dynamical ensembles of configurations with respect to the distribution of topological density have been demonstrated. The instanton-like features are seen to become stronger with more and more iterations of (8). The resemblance to instantons was stated [15] by a close correlation – maximum by maximum of the modulus of the topological density – between the "instanton size", determined by the curvature of $|q(x)|$ in the maximum position x_0 of the cluster, and the value of the density $|q(x_0)|$.

The local lattice operator [16] to represent the topological density for the stout-link smeared configurations is based on a highly improved field-strength tensor,

$$F^{imp}_{\mu\nu}(x) = k_1 C^{(1,1)}_{\mu\nu}(x) + k_2 C^{(2,2)}_{\mu\nu}(x) + k_3 C^{(1,2)}_{\mu\nu}(x) + k_4 C^{(1,3)}_{\mu\nu}(x) + k_5 C^{(3,3)}_{\mu\nu}(x) \tag{9}$$

with

$$\begin{aligned} k_1 &= \frac{19}{9} - 55k_5\ , \\ k_2 &= \frac{1}{36} - 16k_5\ , \\ k_3 &= -\frac{32}{45} + 64k_5\ , \\ k_4 &= \frac{1}{15} - 6k_5\ , \end{aligned} \tag{10}$$

and with

$$C^{(nm)}_{\mu\nu}(x) = \frac{1}{8}\left(W^{(n,m)}_{\mu\nu}(x) + W^{(m,n)}_{\mu\nu}(x)\right) \tag{11}$$

being a symmetrized "clover sum" of $(n\times\hat{\mu}, m\times\hat{\nu})$ Wilson loops around the site x. A 3-loop improved field strength tensor can be achieved chosing $k_5 = 1/90$, such that $k_3 = k_4 = 0$. The topological charge density is then represented in the form

$$q_{sm}(x) = \frac{g^2}{16\pi^2}\mathrm{Tr}\ \left(F_{\mu\nu}\tilde{F}_{\mu\nu}\right)\ . \tag{12}$$

n_{sw}	$Q=-8$	$Q=0$	$Q=-1$	$Q=-7$	$Q=0$
1	0.9954	-0.0001	1.0054	0.6442	0.0000
2	0.9634	-0.0001	-21.5369	0.7987	-0.0001
3	0.9494	-0.0001	3.6497	0.8990	-0.0001
4	0.9585	-0.0002	1.8690	0.9485	-0.0001
5	0.9760	-0.0004	1.4537	0.9728	-0.0001
6	0.9903	-0.0008	1.2736	0.9843	-0.0002
7	0.9982	-0.0015	1.1725	0.9894	-0.0004
8	1.0010	-0.0030	1.1105	0.9915	-0.0006

TABLE I: Table of Z_{sm} values for the initial five configurations. The normalization procedure is only valid for $Q \neq 0$ and works best for large $|Q|$. The fluctuating values for the configuration with $Q=-1$ occuring at $n_{sw}=2$ are due to Q_{sm} being approximately 0 at this point.

III. MATCHING STOUT-LINK SMEARING TO OVERLAP FILTERING

A. Matching the two-point correlator

The two-point correlators for stout-link smearing and overlap filtering are matched using a minimization of the sum of the absolute difference between the correlators. That is, we compute

$$\min\left(\sum_x |\langle q(x)q(0)\rangle_{sm} - \langle q(x)q(0)\rangle_{\lambda_{cut}}|\right) \tag{13}$$

as a function of the number of smearing sweeps, n_{sw}, for fixed λ_{cut}.

The topological charge of each overlap filtered configuration is integer valued because they satisfy the Atiyah-Singer index theorem (4). For stout-link smearing it can take up to 10 sweeps of smearing to achieve an integer charge on these $16^3 \times 32$ lattices. In order to compare overlap filtering and stout-link smearing for $n_{sw} < 10$ in a fair way a non-perturbative normalization is applied. Given that we know the topological charge Q from the overlap configurations, we calculate, for each number of smearing sweeps n_{sw}, a normalization factor Z_{sm} via

$$Q = Z_{sm} \sum_x q_{sm}(x)\,, \tag{14}$$

and $q_{sm}(x)$ is then normalized through $q_{sm}(x) \to Z_{sm}\, q_{sm}(x)$. This ensures that $Q_{sm} = Q$. We also experimented with an alternate normalization where we matched the absolute values of the topological charge density, however this proved less fruitful.

Typical values of Z_{sm} are provided in Table I. For obvious reasons, it is only possible to extract a Z_{sm} factor for $Q \neq 0$, and the procedure works best for Q far from zero. Consequently, the best results are found for the configurations where $Q=-7$ and -8, where the Z_{sm} values rapidly approach 1. This is also the case for the configuration with $Q=-1$, however Z_{sm} fluctuates at $n_{sw}=2$, which is due to Q_{sm} being approximately 0 at this point.

In Table II we present the best matches for the two-point correlators between the filtered overlap densities and the stout-link smeared gluonic densities. Configurations have been used for which the unfiltered overlap topological density (full density) has been measured. The correlators of the fermionic topological density including all known modes, with $\lambda_{cut} = 634$ MeV, with $\lambda_{cut} = 400$ MeV and with $\lambda_{cut} = 200$ MeV are matched against the smeared gluonic correlators.

We show in Fig. 1 the two-point correlator of the topological density for a single configuration represented by the unfiltered fermionic topological density (full density) of Eq. (2) of the equilibrium configuration on one hand and for the gluonic definition of Eq. (12) after 5 smearing steps. It is

λ_{cut}	$Q=-8$	$Q=0$	$Q=-1$	$Q=-7$	$Q=0$
full density	005 005	005 —	005 005	005 004	005 —
all known modes	039 039	043 —	036 036	038 037	034 —
634 MeV	052 052	064 —	048 048	055 055	048 —
400 MeV	127 127	183 —	109 108	139 138	115 —
200 MeV	248 247	300 —	232 232	300 300	271 —

TABLE II: The best matches for the two-point correlators of five different configurations as determined by Eq. (13). For each configuration, the two columns give the number of smearing sweeps that correspond to the best match for a given level of UV filtering. In each case the left column gives the best match for the unnormalised gluonic density and the right column gives the best match for the gluonic density normalised with Z_{sm} (see text). The right columns for the $Q=0$ configurations are absent because the normalization procedure fails in these cases.

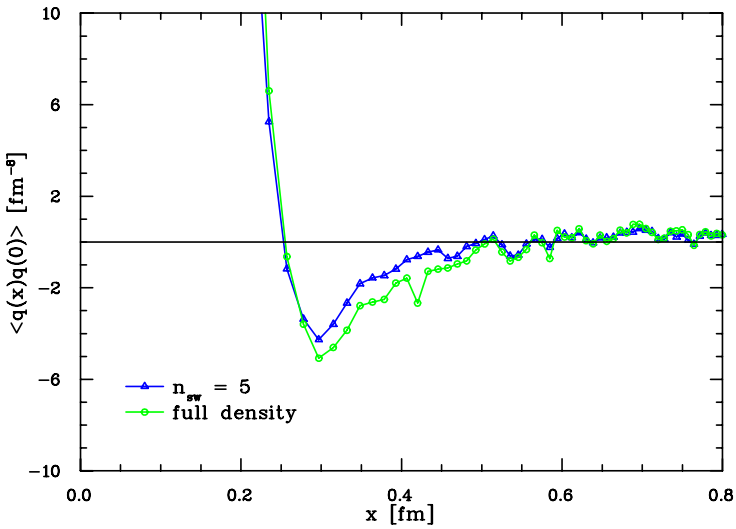

FIG. 1: The two-point function of the fermionic topological density for one configuration shown without mode truncation compared with the bosonic definition after 5 steps of smearing.

remarkable that the two correlators follow each other's fluctuations at larger distance. There is some difference in normalization of the negative peak. This configuration has $Q_{ferm}=-8$, and the gluonic definition gives $Q_{sm}=-8.19$. In this case the "non-perturbative" renormalization would even slightly increase the difference between the curves as the three curves in Fig. 2 show.

In Fig. 3 the density-density two-point correlator for the same configuration is compared for an ultraviolet cutoff $\lambda_{cut}=634$ MeV for the fermionic, overlap definition and the gluonic definition after 52 smearing steps. The filtered correlators match perfectly. The third curve shows the correlator with the gluonic definition after 45 smearing steps. This refers to the case of an optimal point-by-point matching of the densities, as discussed in the next section. The corresponding correlator is somewhat higher and steeper because it uses slightly less smearing iterations.

Fig. 4 shows the same configuration for a lower ultraviolet cutoff $\lambda_{cut}=400$ MeV. After 127 smearing steps the correlator for the gluonic definition fits the correlation function perfectly. Somewhat less smearing steps (103), again optimally fitting the fermionic topological density point by point, tend to overestimate the correlator.

All smeared correlators discussed above were generated using a smearing parameter of $\rho_{sm}=0.06$.

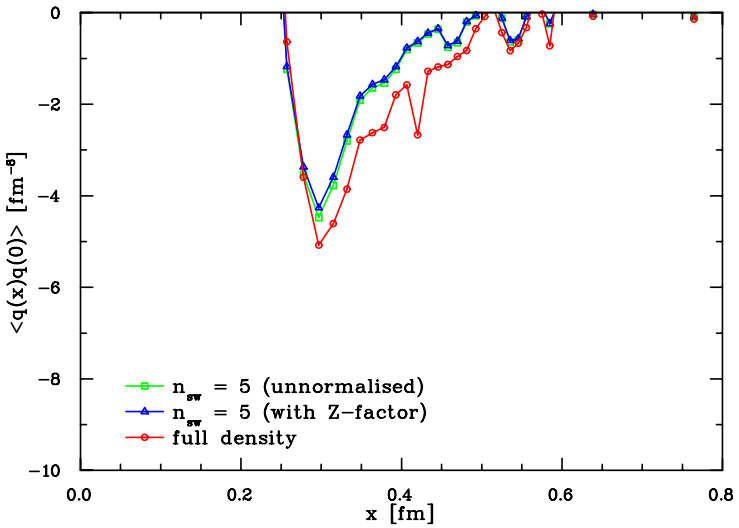

FIG. 2: The same as in Fig. 1 with the effect of the renormalization factor $Z_{sm} = Q_{ferm}/Q_{sm}$ also shown. ($Q_{ferm} = 8$, $Q_{sm} = 8.19$)

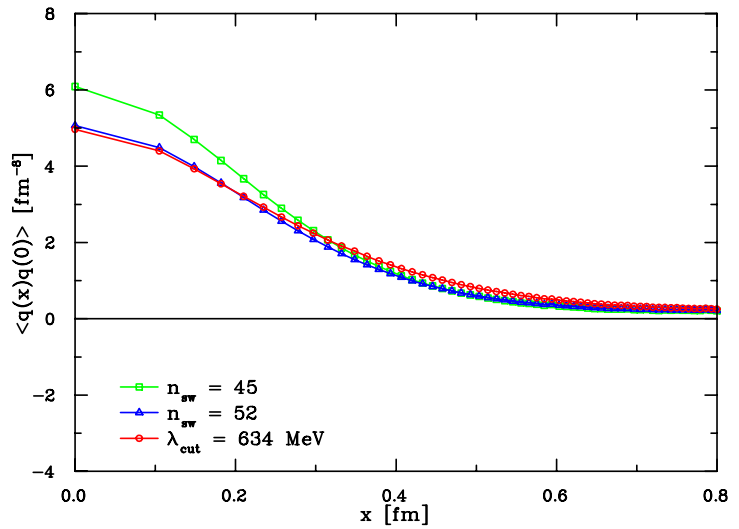

FIG. 3: The two-point function of the fermionic topological density with an UV cutoff at $\lambda_{cut} = 634$ MeV compared with the bosonic definition after 52 steps of smearing when the correlator is fitted best. Smearing after 45 steps leads to the best global matching of the density $q_{\lambda_{cut}}$ with $\lambda_{cut} = 634$ MeV, but the correlator is steeper.

By using a different value for ρ_{sm} it is possible that a different number of smearing sweeps will provide the best fit. This is because the amount of smearing applied to a gauge field is proportional to $\rho_{sm}\, n_{sw}$. By varying ρ_{sm} as well as the number of sweeps one has greater fine-grained control over the matching. Using a variable ρ_{sm}, but holding $n_{sw} = 5$ fixed, and applying this to the same configuration considered previously we find that $\rho_{sm} = 0.055$ provides the best match for the unfiltered topological density.

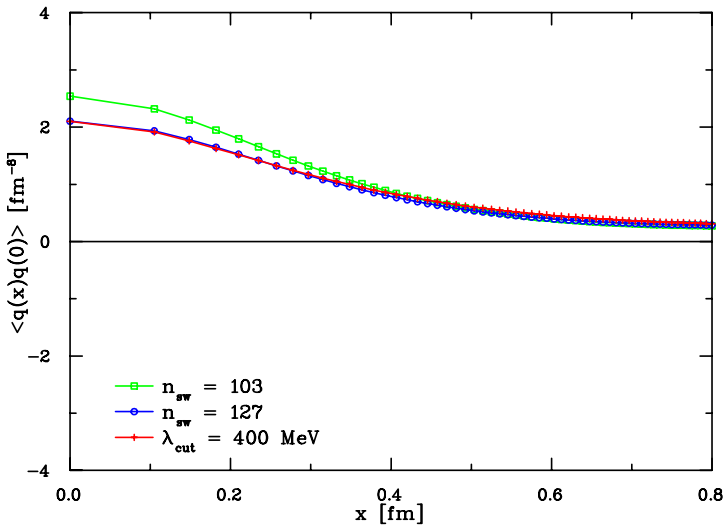

FIG. 4: The same as Fig. 3 with an UV cutoff at $\lambda_{cut} = 400$ MeV fitted best by the bosonic definition after 127 steps of smearing. Smearing after 103 steps leads to the best global matching of the densities, but the correlator is steeper.

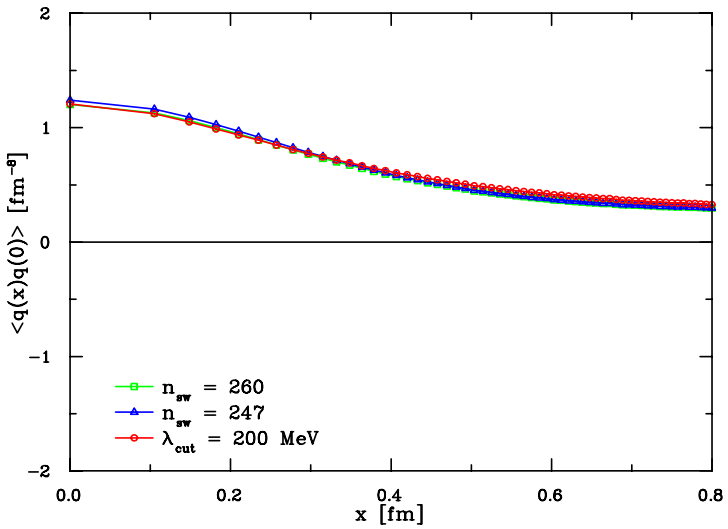

FIG. 5: The same as Figs. 3 and 4, now with an UV cutoff at $\lambda_{cut} = 200$ MeV fitted best by 248 sweeps of smearing. 260 sweeps of smearing gives the best match for the topological charge densities.

A comparison of some different values for for the smearing parameter is provided in Fig. 6. As expected, increasing ρ_{sm} results in a suppression of the negativity of the two-point correlator. Although $\rho_{sm} = 0.055$ provides the best match through a minimization of the sum of the differences in the two-point functions, $\rho_{sm} = 0.06$ gives the best match for the x-intercept. The two-point function for this larger ρ_{sm} also appears to have a similar shape to the two-point function of the full fermionic topological density.

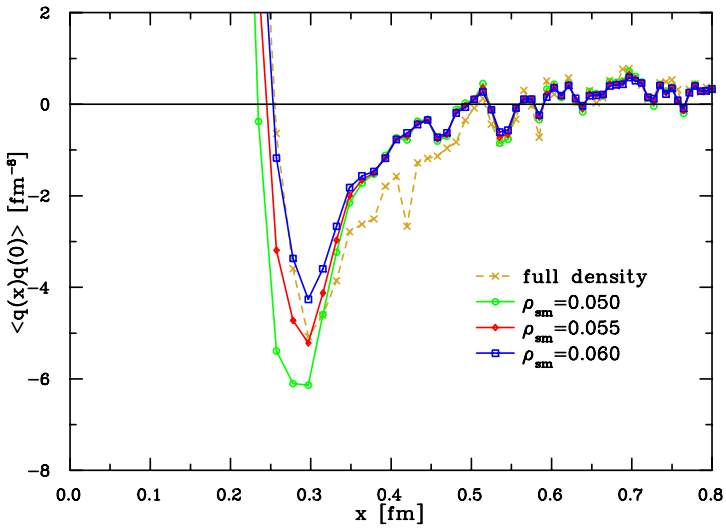

FIG. 6: A comparison of the smeared two-point function for three different values of the smearing parameter, ρ_{sm}. The configuration shown is the same as that used in the previous figures. A best match as dictated by Eq. (13) is given by $\rho_{sm} = 0.055$, however $\rho_{sm} = 0.06$ gives the best match for the x-intercept.

λ_{cut}	$Q=-8$	$Q=0$	$Q=-1$	$Q=-7$	$Q=0$
full density	300 005	300 —	300 006	300 005	300 —
all known modes	037 036	037 —	035 035	035 035	033 —
634 MeV	045 045	048 —	044 044	048 048	044 —
400 MeV	103 103	098 —	103 103	087 087	093 —
200 MeV	261 260	300 —	236 236	192 191	187 —

TABLE III: Best matches for $q(x)$ between the filtered overlap densities and smeared gluonic densities. The left columns contain the best matches with the unnormalised gluonic densities, and the right columns contain the best matches when including the Z_{sm} factor. We see the importance of the Z_{sm} normalization factor when attempting the match the full fermionic density. The right columns are absent for the $Q = 0$ configurations because the normalization method does not work for this Q.

B. Matching the fermionic and gluonic topological density point by point

We now aim to match the filtered fermionic densities with the smeared gluonic densities through a point-by-point matching of the respective topological charge densities $q_{\lambda_{cut}}(x)$ and $q_{sm}(x)$. Given some filtered fermionic topological charge density we compare it against the gluonic density $q_{sm}(x)$ after some number of sweeps by calculating the absolute value of the difference between the respective q at each x. To find the best match we compute the minimum of the sum of the differences,

$$\min \left(\sum_x |q_{sm}(x) - q_{\lambda_{cut}}(x)| \right) , \tag{15}$$

as a function of the number of smearing sweeps, n_{sw}, for fixed λ_{cut}. The non-perturbative normalization of Eq. (14) will also be applied. The best matches are presented in Table III. For a small number of sweeps the importance of the Z_{sm} normalization is apparent. Visualizations of some configurations are shown later in Section IV.

C. Towards the no-smearing limit

Increased smearing leads to flattening of the Euclidean two-point function. It follows that less sweeps of smearing leads to an increasing negative dip in the correlator, and we now study the behaviour of the two-point function in the limit $n_{sw} \to 0$. After only one or two sweeps of smearing there is a non-trivial renormalization that must be applied to the topological charge density. From Table I we see that after three smearing iterations the Z_{sm} factors for the $Q = -7$ and $Q = -8$ configurations are in relatively good agreement. We can therefore study the correlator for $n_{sw} \geq 3$, averaging over these two configurations.

Such a comparison leads to a series of correlators which are displayed in Fig. 7. The x-intercept also moves further towards zero.

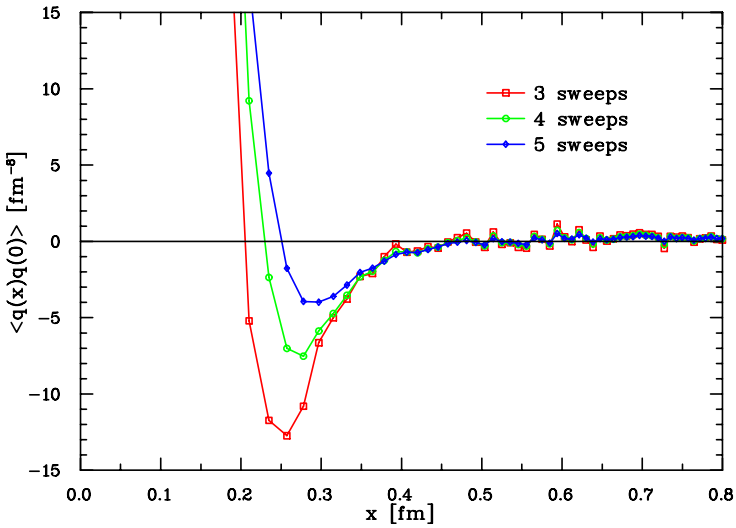

FIG. 7: The two-point function as a function of smearing sweeps. The correlator has been averaged over the two configurations with $Q = -7$ and $Q = -8$. Both charge densities were normalised by an average of the Z_{sm} values for the two configurations. As the number of sweeps is decreased the negative dip increases in magnitude and the x-intercept moves further toward zero.

IV. COMPARISON OF TOPOLOGICAL CLUSTERS

A. Clusters of both topological densities compared for weak stout-link smearing

Using the matching of Eq. (15) we are able to directly compare the overlap topological charge density with some level of UV filtering to a given number of stout-link smearing sweeps. In an early stadium of stout-link smearing the topological density does not yet show classical, instanton-like features. What is meant by "instanton-like features" and how they gradually emerge from stout-link smearing is illustrated for a configuration with $Q = -1$ in Fig. 8. The solid lines represent the relation

$$|q(x_0)| = \frac{6}{\pi^2 \rho_{inst}^4} \,, \tag{16}$$

typical for the (anti)instanton solution, between the gluonic topological charge density in the maxima x_0 of the modulus of the density $|q_{sm}(x)|$ and the "instanton radii" ρ_{inst} obtained from a fit of the curvature of the action density in the points neighbouring x_0. The upper plot has to be considered with a grain of salt because a closer look at the maxima reveals a substantial lack of isotropy of the

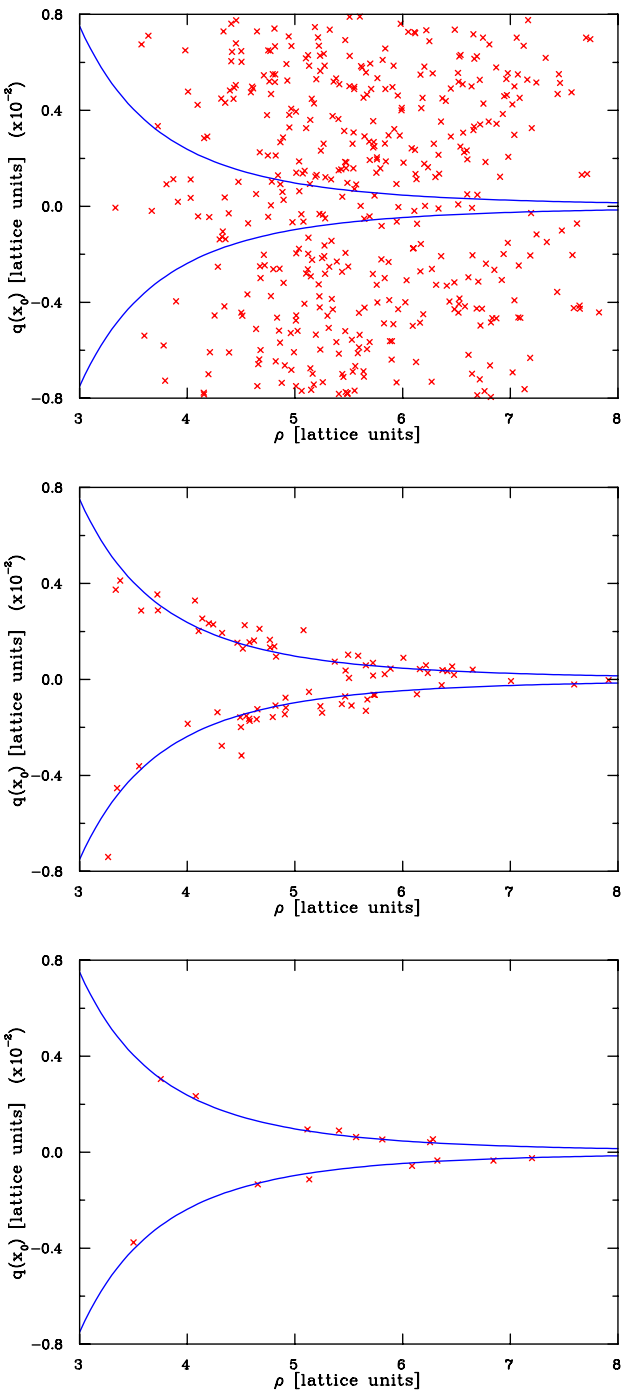

FIG. 8: Three scatterplots showing the increasing instanton-like correlation between the gluonic topological charge density in the maxima x_0 of its modulus $|q_{sm}(x)|$ and the "instanton radii" ρ_{inst} (see text). The solid lines represent the (anti)instanton-like relation between the two cluster parameters. The upper plot shows a huge number of maxima after 5 smearing steps, without any relation between density and size. The middle and bottom plots show a decreasing number of maxima and an inreasing accuracy of the instanton-like relation after 40 and 200 smearing steps, respectively.

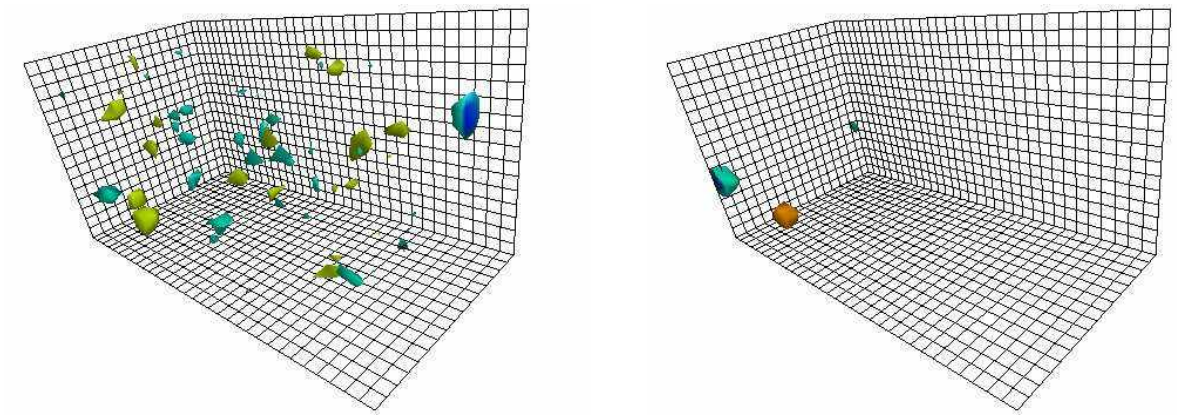

FIG. 9: The gluonic topological charge density very close to the maxima in some timeslice of the same configuration as analyzed in Fig. 8 after 5 (left) and 40 stout-link smearing iterations (right). In color online: negative density blue/green, positive density red/yellow. In grey-scale: negative density dark, positive density light.

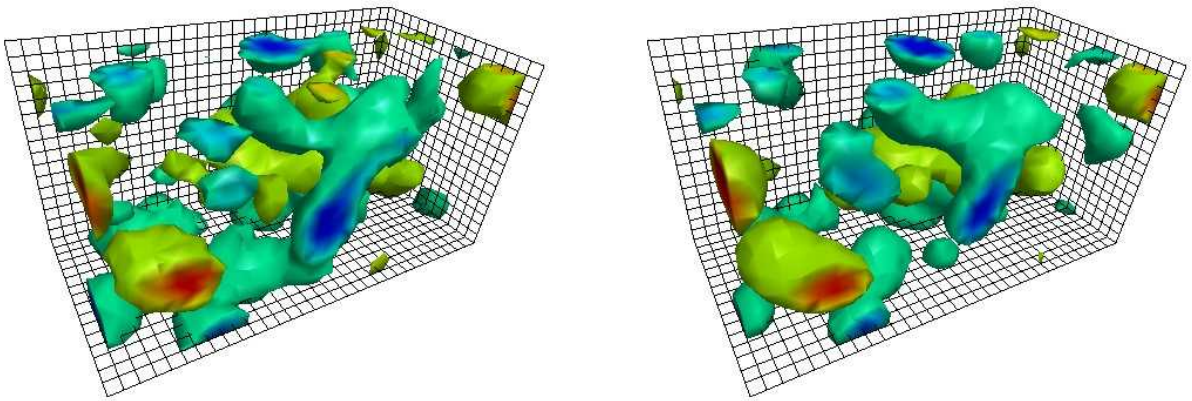

FIG. 10: The fermionic topological charge density of a $Q = 0$ configuration with $\lambda_{cut} = 634$ MeV (left) compared with 48 sweeps of over-improved stout-link smearing (right). In color online: negative density blue/green, positive density red/yellow. In grey-scale: negative density dark, positive density light.

peaks of topological density which is however implicitely assumed in the fits of ρ_{inst}. The marked difference in this respect between 5 and 40 smearing steps is visible in Fig. 9 showing a certain timeslice of the same configuration as in Fig. 8.

For a moderate amount of smearing and filtering, respectively, the two topological density definitions are faithfully exhibiting the outstanding clusterization of charge, provided the cut-off λ_{cut} and the number of stout-link smearing steps are optimally tuned to each other. This is exemplified by Fig. 10 which shows the same time-slice of a $Q = 0$ configuration, on the left-hand side portrayed by the overlap-fermionic topological density with $\lambda_{cut} = 634$ MeV and on the right-hand side by the gluonic topological density after 48 stout-link smearing steps.

In Fig. 11 we show the fermionic density of the $Q = -8$ configuration, with $\lambda_{cut} = 400$ MeV and the gluonic density after 103 stout-link smearing steps. In this stadium of smearing, the bias in favor of classical lumps is already visible.

Besides the similarity between the two methods, the tendency towards classical lumps becomes obvious in Fig. 12. This figure shows the $Q = -7$ configuration with a cutoff of $\lambda_{cut} = 200$ MeV.

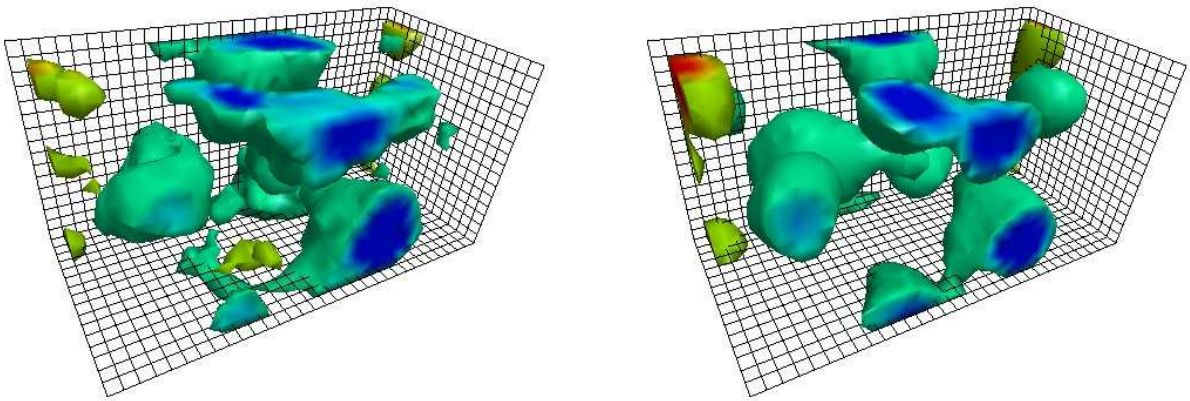

FIG. 11: The fermionic topological charge density of a $Q = -8$ configuration with $\lambda_{cut} = 400$ MeV (left) compared with 103 sweeps of over-improved stout-link smearing (right). In color online: negative density blue/green, positive density red/yellow. In grey-scale: negative density dark, positive density light.

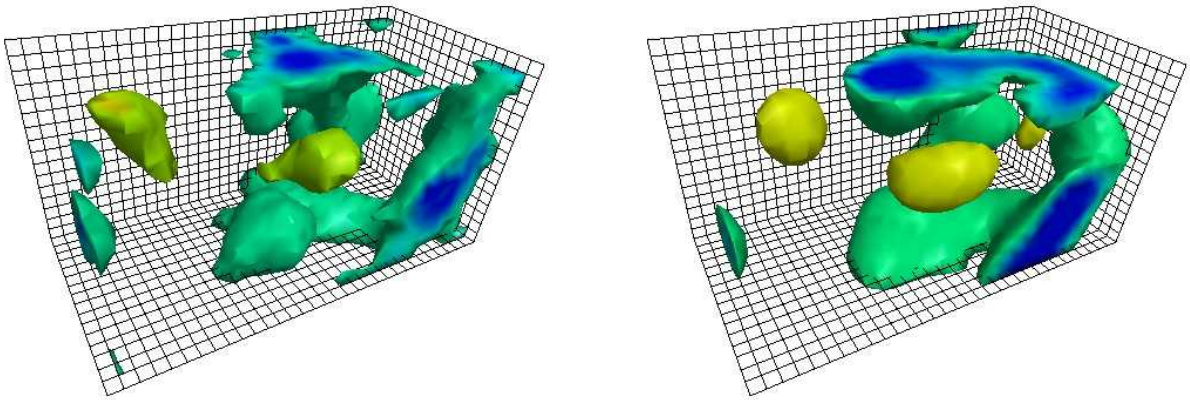

FIG. 12: The fermionic topological charge density of a $Q = -7$ configuration with $\lambda_{cut} = 200$ MeV (left) compared with 192 sweeps of over-improved stout-link smearing (right). In color online: negative density blue/green, positive density red/yellow. In grey-scale: negative density dark, positive density light.

At this level of UV filtering the best match is provided by 193 sweeps of over-improved stout-link smearing. In this stadium of smearing, in particular because of the over-improved action built into the smearing, the minority positive charge has become stabilized compared with what the fermionic view shows.

B. Zero modes and lowest non-zeromodes and the instanton content after long smearing

For long smearing with essentially more than 100 smearing steps, the similarity of the topological densities slowly becomes less perfect. Still, the position of the gluonic topological lumps is not completely arbitrary from the point of view of the original configuration. The zero modes (if $Q \neq 0$) and the lowest non-zero modes contain a high predictive power over where these lumps will appear.

For 200 smearing steps, this is illustrated in Fig. 13 by a $Q = -1$ configuration. In the left panel the gluonic topological density is shown, in the right panel the scalar density of the zero mode. The

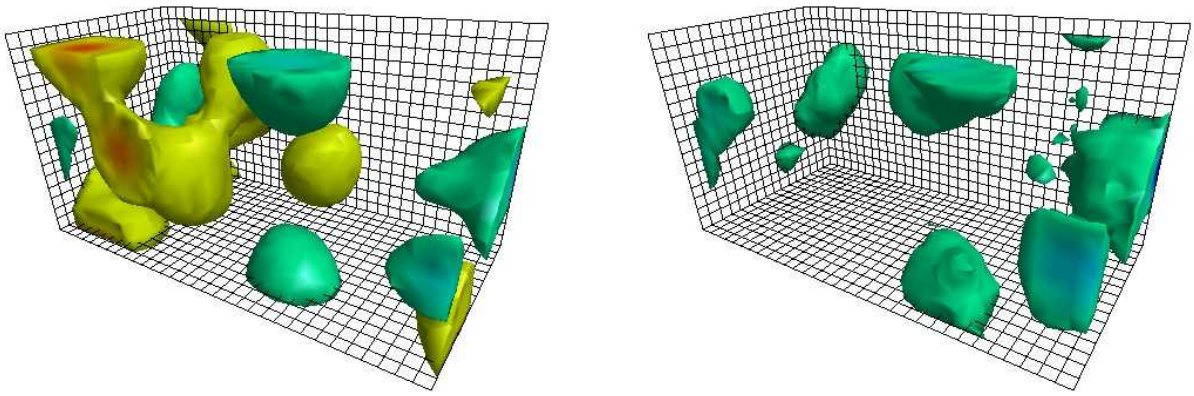

FIG. 13: The gluonic topological charge density after 200 smearing sweeps (left) and the scalar density of the zero mode (right) for a $Q = -1$ configuration. One can see how the zero mode extends over only regions of negative charge. All extended sign-coherent objects seen are good local approximations to instantons or anti-instantons in the centre. In color online: negative density is blue/green, positive density is red/yellow (left), and scalar density is blue/green (right). In grey-scale: negative density dark, positive density light (left).

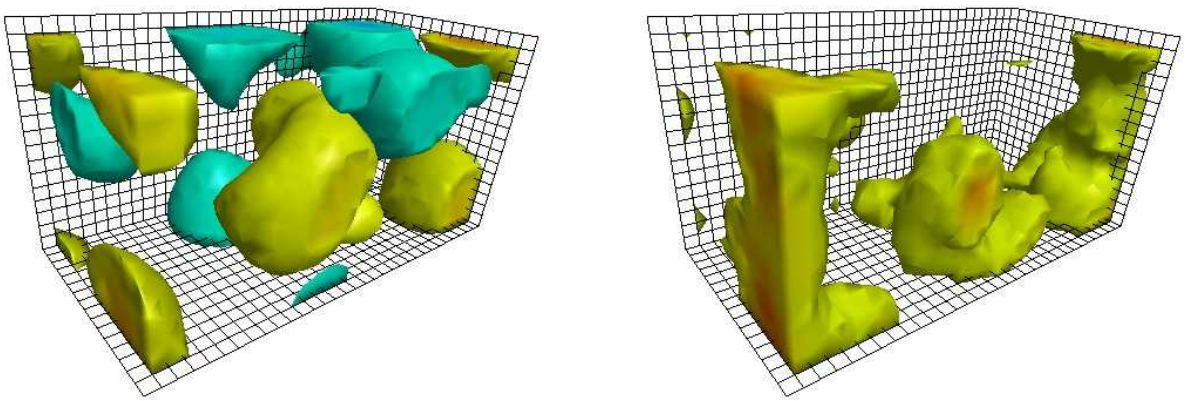

FIG. 14: The gluonic topological charge density after 200 smearing sweeps (left) and the scalar density of the zero mode (right) for a $Q = 1$ configuration. In this case the high density regions of the zero mode are centred on lumps of positive charge. Again all objects are good approximations to classical instantons. In color online: negative density is blue/green, positive density is red/yellow (left), and scalar density is red/yellow (right). In grey-scale: negative density dark, positive density light (left).

zero mode covers three distinct centers of topological charge of appropriate sign only in the selected time-slice. Two more examples of total charge $Q = \pm 1$ are shown in Figs. 14 and 15. One sees that the zero mode does not always cover all regions of appropriate charge. In other words, the gluonic version of the topological charge density for some clusters - even in a late stadium of smearing - may be built by non-zero modes. This leads us to revise the naive expectations according to which each zero mode would be residing on one lump of excess topological charge, for which a cluster charge of $Q_{cl} = \pm 1$ would be suggested by the instanton model. In fact, in Ref. [18] it has been demonstrated that the zero modes typically are simultaneously carried by a moderate number of centers below the peak density, before they start percolating throughout the whole lattice at an even lower level of the scalar density. Here we additionally learn that all theses centers are marked by lumps of topological

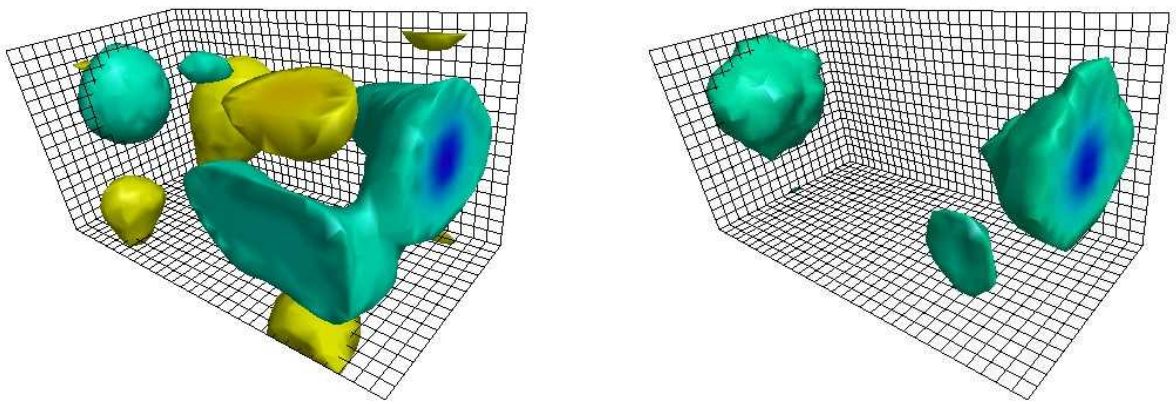

FIG. 15: The gluonic topological charge density after 200 smearing sweeps (left) and the scalar density of the zero mode (right) for another $Q = -1$ configuration. The high density regions of the zero mode are again centred on lumps of negative charge. All topological objects are good approximations to classical instantons. In color online: negative density is blue/green, positive density is red/yellow (left), and scalar density is blue/green (right). In grey-scale: negative density dark, positive density light (left).

charge of appropriate sign, however not necessarily all lumps are covered.

For these same three configurations we now consider the distribution of the lowest non-zero modes. Starting with the first $Q = -1$ configuration, we present the scalar and pseudoscalar densities of the first non-zero mode in Fig. 16. One sees that the pseudoscalar density, according to its local chirality, highlights certain parts of the topological lumps with appropriate sign of charge, and leaves others (for other low-lying modes).

The densities for the next two $Q = 1$ and $Q = -1$ configurations are shown in Figs. 17 and 18. In the instanton model, a whole band of almost-zero modes is generated by diagonalizing the Dirac operator in the field of a superposition of n_+ instantons and n_- anti-instantons in the basis of linear combinations of the $n_+ + n_-$ zero modes corresponding to the case of infinite diluteness. Apart from the remaining $|Q|$ zero modes, the almost-zero modes are expected to bridge at least one pair of instanton and anti-instanton with the scalar density peaking on top of the topological charge lumps and the pseudoscalar density peaking with the appropriate sign there. Qualitatively, this is visible in Figs. 16, 17 and 18.

V. CONCLUSIONS AND OUTLOOK

In this paper we have confronted the overlap-fermionic topological charge density and the improved gluonic topological charge at different levels of ultraviolet smoothing, realized in one case by a truncation of the mode expansion at λ_{cut} and in the other case by a certain number of smearing steps applied to the gauge field in order to wipe out ultraviolet fluctuations. These two views of getting the infrared topological structure of the gauge field correspond to each other. A similar result, however for APE smearing and a different improved Dirac operator, has been found in Ref. [23, 24]. In the present paper this has been confirmed for two other specific realizations of both methods, using the massless overlap Dirac operator [2] on one hand and stout-link smearing with respect to an over-improved Symanzik type action [15] on the other. These two methods have their respective advantages compared to the approximate solution [21, 22] of the Ginsparg-Wilson relation and APE smearing [28].

In this paper, the comparison has been made more complete and detailed, based first on the density-density two-point function and second on a point-by-point matching of the respective topological densities. The correspondence between the ultraviolet cutoff λ_{cut} of the overlap analysis and the number of smearing steps justifies the use of over-improved stout-link smearing, which is computationally less

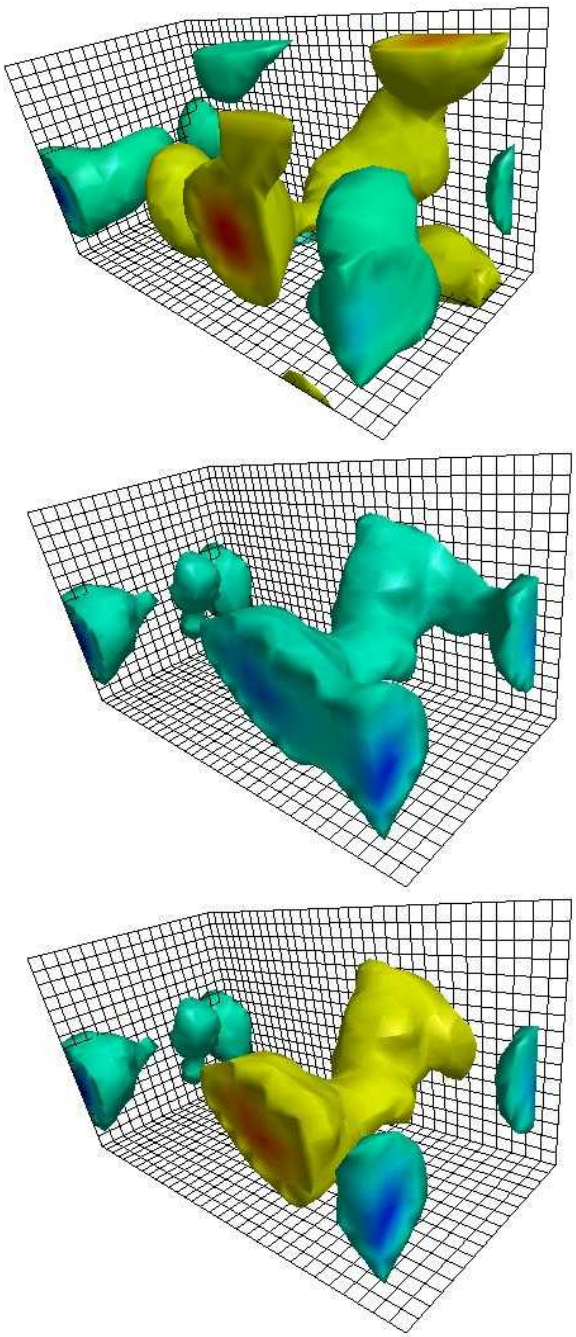

FIG. 16: The scalar (middle) and pseudoscalar (bottom) density of the first non-zero mode for the $Q = -1$ configuration shown previously in Fig. 13, along with the gluonic topological charge density after 200 sweeps of smearing (top). One sees how the scalar density extends over objects of differing charge, but that the regions of alternate charge are realized by the local chirality of the pseudoscalar density. In color online: negative density is blue/green, positive density is red/yellow (top), positive chirality is blue/green and negative chirality is red/yellow (bottom). In grey-scale: negative density dark, positive density light (top), and positive chirality dark, negative chirality light (bottom).

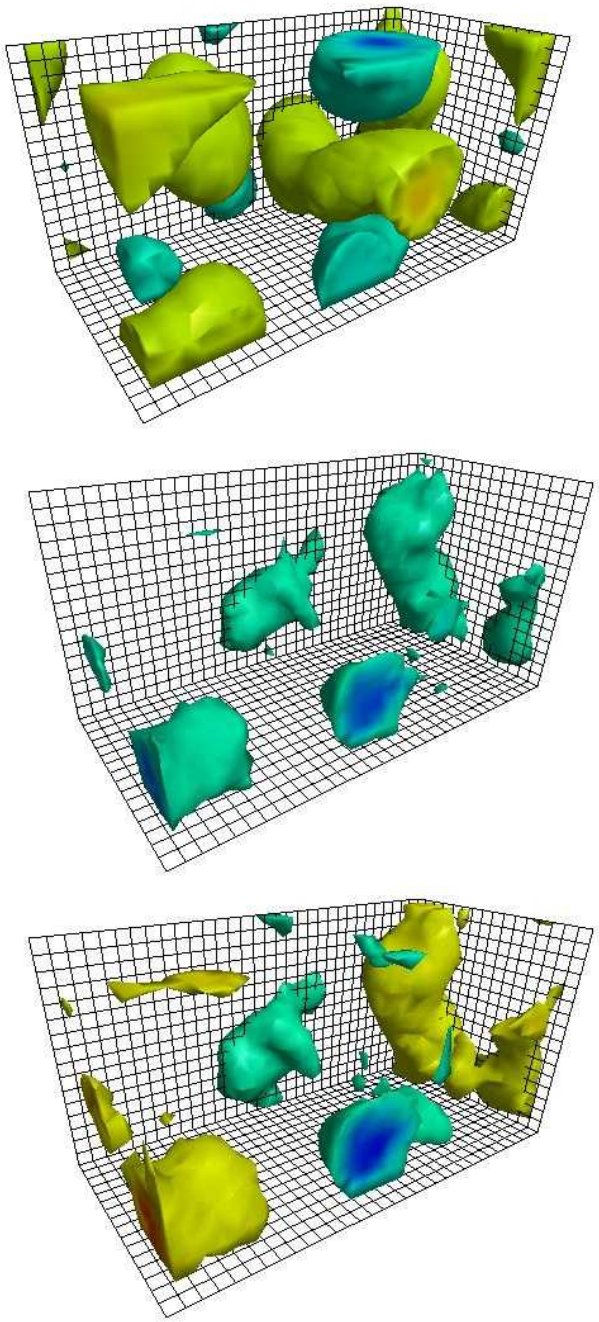

FIG. 17: The scalar (middle) and pseudoscalar (bottom) density of the first non-zero mode for the $Q = 1$ configuration shown previously in Fig. 14, along with the gluonic topological charge density after 200 sweeps of smearing (top). Again, the scalar density extends over objects of differing charge, and the regions of alternate charge are revealed by the local chirality of the pseudoscalar density. In color online: negative density is blue/green, positive density is red/yellow (top), positive chirality is blue/green and negative chirality is red/yellow (bottom). In grey-scale: negative density dark, positive density light (top), and positive chirality dark, negative chirality light (bottom).

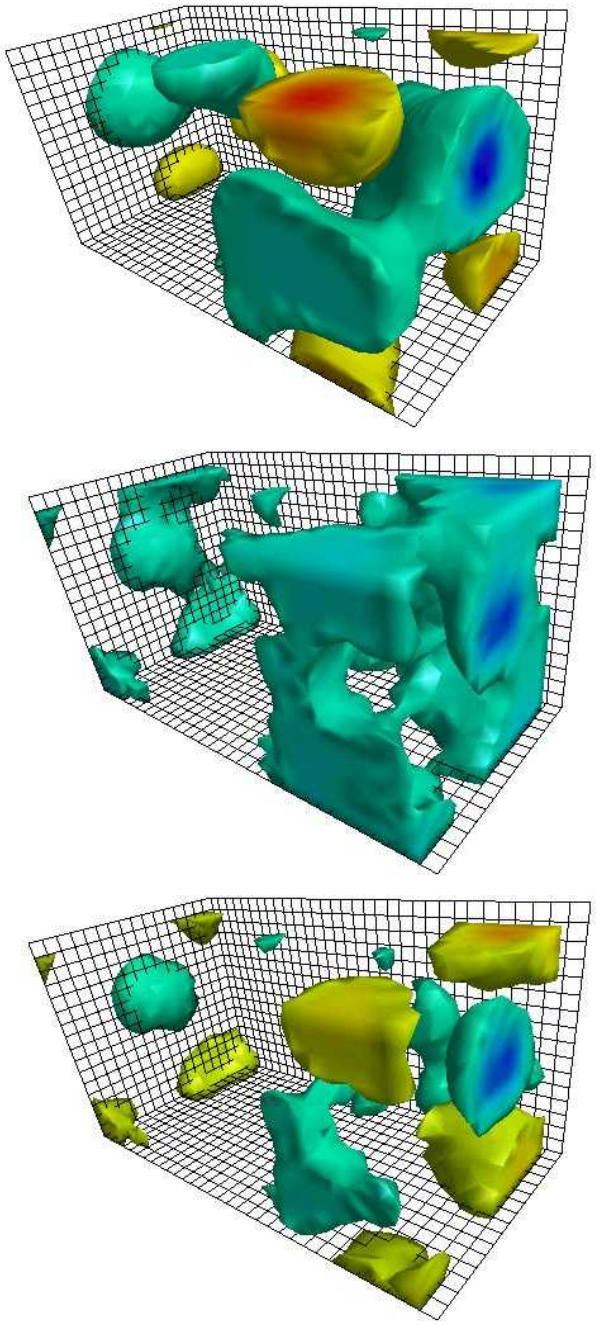

FIG. 18: The scalar (middle) and pseudoscalar (bottom) density of the first non-zero mode for the $Q = -1$ configuration shown previously in Fig. 15, along with the gluonic topological charge density after 200 sweeps of smearing (top). Again, the scalar density extends over objects of differing charge, and the regions of alternate charge are revealed by the local chirality of the pseudoscalar density. In color online: negative density is blue/green, positive density is red/yellow (top), positive chirality is blue/green and negative chirality is red/yellow (bottom). In grey-scale: negative density dark, positive density light (top), and positive chirality dark, negative chirality light (bottom).

demanding, in the analysis of topological vacuum structure. This is of particular interest when investigating the differences between the vacuum structure of quenched and non-quenched QCD [15, 28].

What we did not yet do in the present paper is the natural next step of formulating a description of the outstanding clusters of topological charge (at each level of ultraviolet smoothing) in terms of an filtered field strength, a possibility also offered by the overlap analysis [6]. Furthermore, one should study the degree of (anti)selfduality of the gauge field and the percolation properties of the corresponding (anti)selfdual domains [6]. Both questions are accessible not only by the fermionic method but also by the gluonic method based on stout-link smearing.

ACKNOWLEDGEMENTS

E.-M. I. acknowledges the support from DFG under the grant FOR 465 / Mu932/2-2. E.-M. I., K. K., G. S. and V. W. thank T. Streuer and Y. Koma for collaboration in earlier stages of the overlap project within this DFG-Forschergruppe. E.-M. I. thanks F. Bruckmann, Ch. Gattringer, M. Müller-Preussker, A. Schäfer and S. Solbrig for collaboration on a similar comparative study within the DFG-Forschergruppe. He is grateful to Lorenz von Smekal for the invitation to Adelaide which was made possible by a grant under the Strategic Research Scheme of the Faculty of Sciences of the University of Adelaide devoted to the collaboration on Infrared QCD between Humboldt University Berlin and Adelaide University.

P. M. and D. L. thank the Australian Partnership for Advanced Computing (APAC) and the South Australian Partnership for Advanced Computing (SAPAC) for generous grants of supercomputer time which have enabled this project. This work is supported by the Australian Research Council.

---

[1] H. Neuberger, Phys. Lett. **B417**, 141 (1998), hep-lat/9707022.
[2] H. Neuberger, Phys. Lett. **B427**, 353 (1998), hep-lat/9801031.
[3] P. Hasenfratz, V. Laliena, and F. Niedermayer, Phys. Lett. **B427**, 125 (1998), hep-lat/9801021.
[4] F. Niedermayer, Nucl. Phys. Proc. Suppl. **73**, 105 (1999), hep-lat/9810026.
[5] I. Horvath et al., Phys. Rev. **D67**, 011501 (2003), hep-lat/0203027.
[6] E.-M. Ilgenfritz et al., Phys. Rev. **D76**, 034506 (2007), arXiv:0705.0018 [hep-lat].
[7] M. Teper, Phys. Lett. **B171**, 86 (1986).
[8] E.-M. Ilgenfritz et al., Nucl. Phys. **B268**, 693 (1986).
[9] P. de Forcrand, M. Garcia Perez, and I.-O. Stamatescu, Nucl. Phys. **B499**, 409 (1997), hep-lat/9701012.
[10] M. Garcia Perez, O. Philipsen, and I.-O. Stamatescu, Nucl. Phys. **B551**, 293 (1999), hep-lat/9812006.
[11] M. Garcia Perez et al., Nucl. Phys. **B413**, 535 (1994), hep-lat/9309009.
[12] F. Bruckmann et al., Phys. Rev. **D70**, 105013 (2004), hep-lat/0408004.
[13] C. Morningstar and M. J. Peardon, Phys. Rev. **D69**, 054501 (2004), hep-lat/0311018.
[14] P. J. Moran and D. B. Leinweber (2008), arXiv:0801.1165 [hep-lat].
[15] P. J. Moran and D. B. Leinweber, PoS **LATTICE 2007**, 383 (2007), arXiv:0710.2380 [hep-lat].
[16] S. O. Bilson-Thompson, D. B. Leinweber, and A. G. Williams, Ann. Phys. **304**, 1 (2003), hep-lat/0203008.
[17] I. Horvath et al., Phys. Rev. **D68**, 114505 (2003), hep-lat/0302009.
[18] E.-M. Ilgenfritz et al., PoS **LATTICE 2007**, 311 (2007), arXiv:0710.2607 [hep-lat].
[19] T. A. DeGrand and A. Hasenfratz, Phys. Rev. **D64**, 034512 (2001), hep-lat/0012021.
[20] F. Bruckmann and E.-M. Ilgenfritz, Phys. Rev. **D72**, 114502 (2005), hep-lat/0509020.
[21] C. Gattringer, I. Hip, and C. B. Lang, Nucl. Phys. **B597**, 451 (2001), hep-lat/0007042.
[22] C. Gattringer, Phys. Rev. **D63**, 114501 (2001), hep-lat/0003005.
[23] F. Bruckmann et al., Eur. Phys. J. **A33**, 333 (2007), hep-lat/0612024.
[24] S. Solbrig et al., PoS **LATTICE 2007**, 334 (2007), arXiv:0710.0480 [hep-lat].
[25] T. L. Ivanenko and J. W. Negele, Nucl. Phys. Proc. Suppl. **63**, 504 (1998), hep-lat/9709130.
[26] Y. Koma et al., PoS **LAT2005**, 300 (2006), hep-lat/0509164.
[27] M. Göckeler et al., Phys. Lett. **B233**, 192 (1989).
[28] A. Hasenfratz, Phys. Lett. **B476**, 188 (2000), hep-lat/9912053.